ADVANCED FUNCTIONAL MATERIALS
www.afm-journal.de

www.MaterialsViews.com

Antimony Induced {112}A Faceted Triangular $GaAs_{1-x}Sb_x$/InP Core/Shell Nanowires and Their Enhanced Optical Quality

Xiaoming Yuan, Philippe Caroff,* Fan Wang, Yanan Guo, Yuda Wang, Howard E. Jackson, Leigh M. Smith, Hark Hoe Tan, and Chennupati Jagadish*

Mid-infrared $GaAs_{1-x}Sb_x$/InP core/shell nanowires are grown coherently with perfectly twin-free zinc blende crystal structure. An unusual triangular InP shell with predominantly {112}A facets instead of {112}B facets is reported. It is found that this polarity preference is due to the surfactant role of Sb, which inhibits InP shell growth rate in the ⟨112⟩A directions. This behavior reveals a new degree of control and tunability allowed in manipulating nanowire facet geometry and polarity in radial heterostructures by a simple means. Tuning the Sb composition in the core yields controllable intense photoluminescence emission in both the 1.3 and 1.5 μm optical telecommunication windows, up to room temperature for single nanowires. The internal quantum efficiency of the core/shell nanowires is experimentally determined to be as high as 56% at room temperature. Transient Rayleigh scattering analysis brings complementary information, revealing the photoexcited carrier lifetime in the core/shell nanowire to be ≈100 ps at 300 K and ≈800 ps at 10 K. In comparison, the carrier lifetime of core-only nanowire is below the detection limit of the system (25 ps). The demonstrated superior optical quality of the core/shell nanowires and their ideal emission wavelength range makes them highly relevant candidates for near-infrared optoelectronic applications.

1. Introduction

III–V semiconductor nanowires (NWs) are high-quality nanoscale building blocks for optoelectronic applications thanks to their exceptional optical quality, cylindrical cavity geometry, and the freedom in band structure engineering offered by their ability to form complex axial and lateral heterostructures.[1,2] These NWs and their heterostructures have been demonstrated to have excellent electronic[3] and optical properties[4–6] in the visible and near-infrared region, and been applied to wrap-gated field effect transistors integrated on Si,[7] small footprint lasers,[8–10] light management in solar cells,[11–14] and integrated light-emitting diodes on Si with superior structural quality.[15,16] NWs applications in the telecommunication range (from 1 to 2 μm) are less developed since strain-free binary heterostructures do not cover that wavelength range. Strain engineering can push binaries such as the InAs/InP system into communication wavelengths,[17,18] but with limitations to very narrow quantum wells or small diameter quantum dots to prevent detrimental strain-induced defect formation. Expanding radial heterostructure to use ternary NW alloys is therefore a natural way to tune emission wavelength while minimizing the strain level.[5,16,19,20] However growth-related challenges of crystal structural perfection and composition homogeneity still impair the development of ternary NWs and their applications.[21,22] $GaAs_{1-x}Sb_x$ NW is considered as a desirable candidate for applications in the near-infrared range due to its high crystal quality, reasonable composition homogeneity with a tunable bandgap from 870 (GaAs) to 1700 nm (GaSb),[23] and proven ability for monolithic integration on silicon.[24] $GaAs_{1-x}Sb_x$ core-only NWs photoluminescence at room temperature is more intense than that of GaAs[25] but still not sufficiently efficient because of its high surface recombination velocity (SRV) which has a value between that of GaAs ($\approx 2.5 \times 10^6$ cm s^{-1})[26] and GaSb (8×10^4 cm s^{-1}).[27] By forming a core/shell structure with a larger bandgap material shell (such as GaAs/AlGaAs), the emission efficiency could be significantly enhanced due to surface passivation.[6] Among the III–V semiconductors, InP is an ideal shell candidate for $GaAs_{1-x}Sb_x$ core as a result of its extremely low SRV.[28] In addition it is lattice-matched to $GaAs_{0.51}Sb_{0.49}$ and has the possibility of forming either a type-I or type-II band alignments depending on the Sb composition. Indeed, record high frequency double heterostructure bipolar transistors (DHBT) reported recently validate

X. Yuan, P. Caroff, F. Wang, Y. Guo, H. H. Tan, C. Jagadish
Department of Electronic Materials Engineering
Research School of Physics & Engineering
The Australian National University
Canberra ACT 2601, Australia
E-mail: xiaoming.yuan@anu.edu.au; philippe.caroff@anu.edu.au
Y. Wang, H. E. Jackson, L. M. Smith
Department of Physics
University of Cincinnati
Cincinnati OH 45221-0011, USA

DOI: 10.1002/adfm.201501467

the very high quality of $GaAs_{1-x}Sb_x$/InP based heterostructures.[29] However, the potential for applications in nanowire optoelectronics has remained relatively unexplored.

In this work, we report the growth of $GaAs_{1-x}Sb_x$ /InP core/shell nanowire via the metal-seeded vapor–liquid–solid (VLS) growth method using metal–organic vapor phase epitaxy (MOVPE). Triangular {112} side facets with unexpected A-polarity are observed and proven to be linked with the presence of Sb acting as a surfactant. Antimony (Sb) has low surface energy (0.358 J m^{-2})[30] and has been often used in altering the crystal growth behavior in layer-by-layer or 3D quantum dots.[31–33] Surfactant effect has also been found to be effective in tuning the crystal structure, faceting, or growth direction in III–V nanowire growth.[23,34–36] This is the first report on the surfactant role of Sb during intentional core–shell NW heterostructure growth. Strong photoluminescence (PL) emission near 1.3 and 1.5 µm is obtained from single NW PL experiment at room temperature. The PL intensity is enhanced by two orders of magnitude in the core/shell structure compared with the bare core and is related to an excellent internal quantum efficiency (IQE) which can be as high as 56% and long photoexcited carrier lifetime (≈800 ps at 10 K).

2. Results and Discussion

2.1. High Crystal Quality of $GaAs_{0.56}Sb_{0.44}$/InP Core/Shell Structure

Figure 1 shows the morphology and crystal structure of the $GaAs_{0.56}Sb_{0.44}$/InP core/shell NWs. After optimized InP shell growth, the NWs exhibit a triangular cross-section shape with smooth sidewalls (Figure 1b,d) instead of a hexagonal shape such as seen for the $GaAs_{1-x}Sb_x$ core (Figure 1a).[23] This indicates anisotropic growth of the InP shell. More images of the the core/shell NWs at different InP shell growth conditions can be found in Figure S1 (Supporting Information). The transmission electron microscopy (TEM) image along the [1-10] zone axis (Figure 1c) shows only thickness contrast with a thicker region along the right hand side. The thicker region (Figure 1c) represents a major side facet of the nanowire based on the triangular geometry observed in the scanning electron microscopy (SEM) top view (Figure 1d). Since the $GaAs_{1-x}Sb_x$ core NWs were grown along the [111]B direction, the right hand side of the nanowire in Figure 1c is determined to be the ⟨112⟩ A directions according to the corresponding selective area diffraction pattern (SADP) (Figure 1e).[37] Thus, the three facets forming the isosceles triangular prism shape of the nanowire are A-polar, as marked in Figure 1d. This result is highly unexpected under PH_3 rich condition. Indeed, although NWs with a triangular shape are common in III–V compounds,[22,37–42] most of the previous papers reported B-polar {112} facets except for GaP nanowires grown at low temperature and low V/III ratio[41] and recently reported Sn seeded GaAs nanowires.[43] The vast dominance of {112}B terminated triangular sidewalls in III–V nanowires is simply attributed to a lower surface energy of the B-polar facets with respect to their A-polar counterparts under group V–rich growth conditions.[44] As a result, A-polar facets grow faster than the B-polar facets and gradually shrink,[45,46] leaving the NWs bound largely by B-polar facets after growth (except in the vicinity of their apexes.[44] No planar faults, twins, or stacking faults, are observed in either the core or the shell.

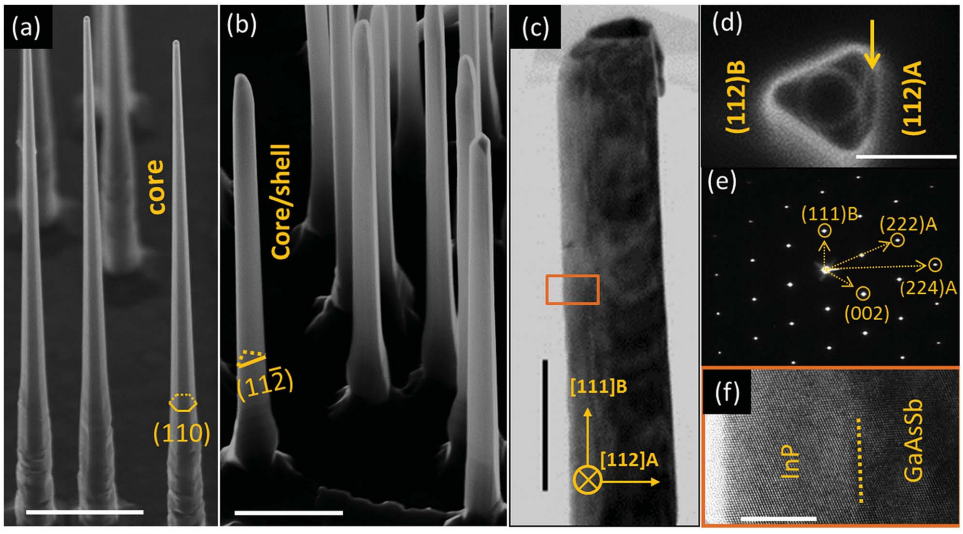

Figure 1. Morphology and crystal structure of the $GaAs_{0.56}Sb_{0.44}$/InP core/shell NWs, showing the triangular shape with {112}A terminated side facets. a) SEM image (45° tilt) of the NWs before InP shell growth with electron beam projected in the [1-10] direction. $GaAs_{0.56}Sb_{0.44}$ NWs have a hexagonal shape with {110} side facets. b) Core/shell NWs have a triangular shape with {112} side facets after InP shell growth at 550 °C for 16 min. c) TEM image of a typical core/shell NW along the [1-10] zone axis shows the thickness contrast with thicker region on the right hand side of the NW. d) Top view of a core/shell nanowire with the arrow indicating the electron projection direction in (c). This shows the right hand side of the NW in (c) represents a facet, either {112}A or {112}B. e) Corresponding SADP in (c) confirms that the right hand side of the NW is [112] A and the triangle shape of core/shell NWs mainly consists of {112}A side facets. f) HRTEM image of (c) shows ZB twin-free structure of both the core and shell. The dotted line indicates the boundary between the core and shell. No dislocation is observed at the interface. Scale bars are 1 µm in (a) and (b), 200 nm in (c), 100 nm in (d), and 10 nm in (f).

The InP shell inherits the zinc blende (ZB) twin free structure from the $GaAs_{1-x}Sb_x$ core, as confirmed by a high-resolution TEM (HRTEM) image (Figure 1f) of the marked region in Figure 1c. No dislocation at the interface between the core and shell is observed.

The unexpected formation of A-polar side facets of InP on $GaAs_{1-x}Sb_x$ core suggests some fundamental changes with respect to other standard III–V core–shell structures reported to date. To push the investigation of this original core–shell formation further, cross-sectional TEM analysis was performed. A typical cross section of the $GaAs_{0.56}Sb_{0.44}$/InP core/shell NW is shown in **Figure 2**a. The interface between the $GaAs_{0.56}Sb_{0.44}$ core and the outer InP shell is indicated by the dotted line. The inner $GaAs_{0.56}Sb_{0.44}$ core shows hexagonal shape with nonpolar {110} facets, in agreement with previous reports on this material system.[23,47] In contrast, the outer InP shell is bound by the polar {112}A facets. Importantly, the InP shell growth rate in the ⟨112⟩A directions is entirely suppressed, which results in the formation of {112}A side facets. The shape of the core/shell structure is further confirmed by energy dispersive X-ray (EDX) composition mapping (Figure 2b). The inner core is hexagonal and shows six As-rich bands along the six ⟨112⟩ directions, in accordance with previous reports.[23,24] The EDX map demonstrates the selective growth of InP shell, resulting in poor coverage of InP on the $GaAs_{0.56}Sb_{0.44}$ core along the ⟨112⟩A directions. This facet-selective growth has been demonstrated for radial inclusion of different quantum structures in both group IV and III–V semiconductor nanowire systems.[48–50] Figure 2c compares the EDX spectrum of the core and shell. No In or P could be detected in the core while trace amount of Ga, As, and Sb are found in the shell. One possible reason explaining the presence of these elements in the shell is the existence of residual Ga, As, and Sb in the vapor due to re-evaporation from the susceptor or walls of the MOVPE reactor. However, since Sb is neither found in the core nor the shell during the subsequent growth of a test GaAs/InP core/shell structure immediately after the $GaAs_{1-x}Sb_x$ growth (see Figure S2, Supporting Information), this possibility is not likely. Instead, atomic interdiffusion between the core and shell during high-temperature growth of the shell could explain the observed alloying.[6] A HRTEM image and the corresponding geometrical phase analysis (GPA) in the marked region in Figure 2a is shown in Figure 2d–f. Dislocations could not be observed from either the HRTEM or GPA mapping, which suggests that InP shell grows coherently without the formation of any misfit dislocations on the $GaAs_{0.56}Sb_{0.44}$ core. This is reasonable since there is only a 0.4% lattice mismatch between the core with nominal 44% Sb and the InP shell. According to GPA

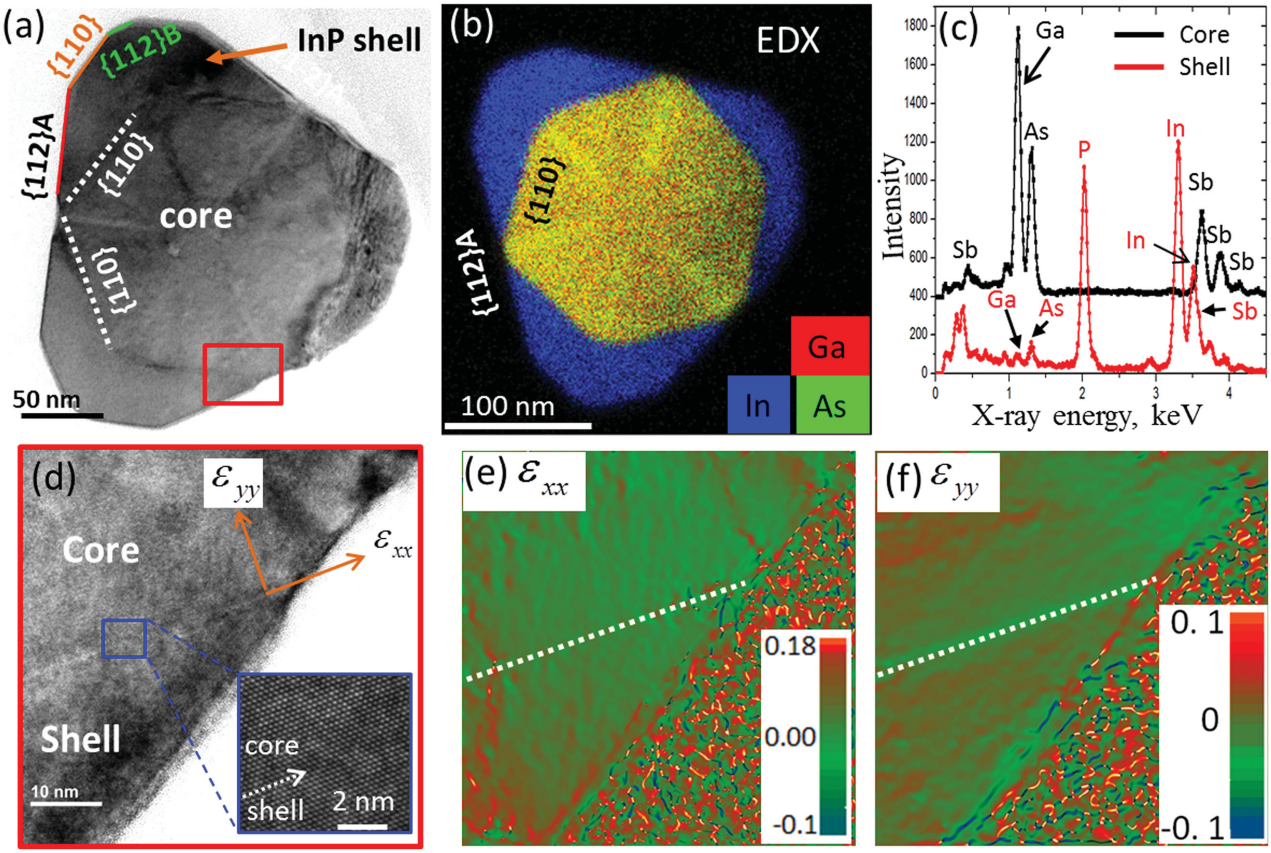

Figure 2. Microstructure and compositional analyses of the core/shell structure. a) TEM image of a typical cross-sectional sample, showing the hexagonal core and truncated triangle shape of the shell. b) Confirmation of the InP shell by EDX mapping. c) Point EDX analysis of core and shell, showing the existence of trace amount of Ga, As, and Sb in the shell. d) HRTEM and e,f) corresponding GPA analysis of the region marked in (a), demonstrating the coherence between the core and shell. Dotted white lines in (a), (d–f) indicate the boundary between the core and shell.

strain mapping, only moderate strain contrast is observed, indicating that the core and shell are close to lattice matched.

Another core/shell sample with lower Sb in the core ($x = 0.29$) shows the same shell growth behavior, indicating that the preference of A-polar {112} facets is not caused by the Sb composition difference or more fundamentally by the strain between the core and shell (see Figure S3, Supporting Information). InP grows smoothly on the core, but it still does not cover the core in the ⟨112⟩A directions. Around 1.5% lattice mismatch exists between the core and shell. The critical thickness at this level of strain between $GaAs_{1-x}Sb_x$ and InP heterostructure is calculated to be around 30 nm, which implies a coherent interface since the InP shell thickness is much smaller for this sample (≈12 nm).[51] Further HRTEM and GPA analysis confirm the coherence (Figure S3e, Supporting Information).

2.2. Surfactant Role of Sb in Forming A-Polar {112} Side Facets

The polarity-driven InP shell growth process is illustrated in **Figure 3**. After switching to the shell growth, InP starts growing on the hexagonal $GaAs_{1-x}Sb_x$ core along the ⟨110⟩ and ⟨112⟩B directions except in the ⟨112⟩A directions. Consequently, the original {110} facets gradually shrink due to the fast growth while the limiting {112}A facets are gradually formed. As the shell growth time increases, the morphology of the core/shell structure evolves from hexagon to truncated hexagon to nearly triangle terminated with {112}A facets. This whole shape evolution process is presented as an animation, made of cross-section TEM images for different shell thicknesses, in Figure S4 (Supporting Information) for InP shell growth from 0 to 40 min.

Figure 3b shows an atomic model of the core/shell structure projected in the [1-10] direction. A- and B-polar {112} surfaces have extra Ga(In)— and As(Sb)— dangling bonds, respectively, as indicated by the black arrow. This results in different surface energies between the {112}A and {112}B facets. Under PH_3 or AsH_3 rich conditions, A-polar surfaces have larger surface energy than B-polar surfaces;[41,44] therefore, they have a larger growth rate according to the Wulff's rule.[45] However, the InP shell on the $GaAs_{1-x}Sb_x$ core only grows along the ⟨112⟩B directions instead of the assumed ⟨112⟩A directions as shown in Figure 3a. One likely reason for this opposite growth trend is the presence of Sb, as the surfactant role of Sb is well known to alter crystal growth.[32,35]

To test this hypothesis, an InP shell is grown with the same optimal shell growth conditions on 100 nm GaAs core which is grown using a two-temperature process to guarantee a pure ZB twin-free structure.[52] In contrast to growths on $GaAs_{1-x}Sb_x$ cores, the InP shell grown on a GaAs core exhibits a hexagonal shape with mainly {110} facets with smaller {112}A and {112}B facets (see Figure S2, Supporting Information). The GaAs core on the other hand has a truncated hexagonal shape formed by the larger {112}B and smaller {112}A facets.[44] Thus, the larger (smaller) {112} facets of the InP shell are determined to be B (A) polar, respectively, as indicated in Figure S2b (Supporting Information). This shape indicates that the growth rate in the ⟨112⟩A directions is larger than in ⟨112⟩B and both growth rates are larger than in ⟨110⟩ directions, which agrees well with the standard hierarchy of surface energies: $\gamma_{\{110\}} < \gamma_{\{112\}B} < \gamma_{\{112\}A}$. In addition, the InP shell growth rate in the ⟨110⟩ directions of the GaAs core (7.1 nm min^{-1}) is over five times larger than that on the $GaAs_{1-x}Sb_x$ core (1.3 nm min^{-1}), suggesting that the driving force for InP shell nucleation on the $GaAs_{1-x}Sb_x$ surface is strongly reduced by the presence of Sb. Considering the fact that Sb is effective in tuning the crystal growth by its surfactant role, including but not limited to suppressing growth rate of Si NWs and changing crystal morphology of GaN and GaSb,[32,35,53] we ascribe the reduced growth rate and triangular shape of InP shell to a reduction of surface energy in the presence of Sb.

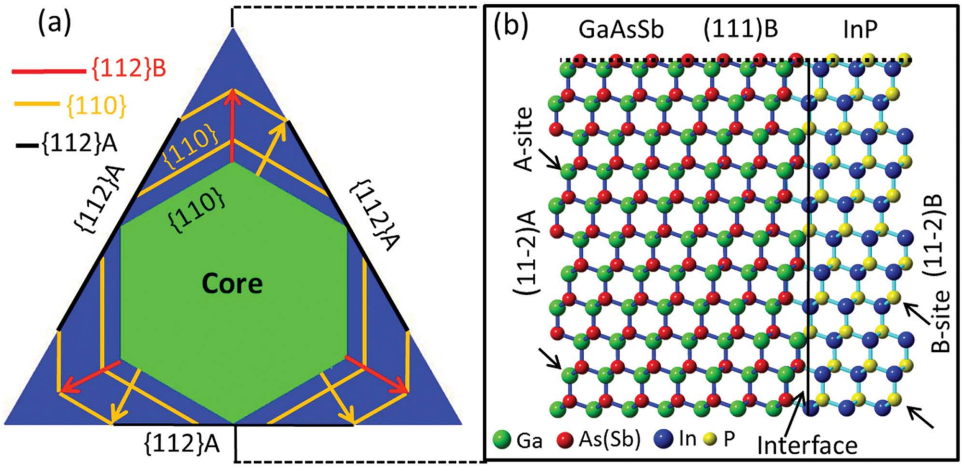

Figure 3. Illustration of the growth behavior of InP shell on a $GaAs_{1-x}Sb_x$ core. a) Schematic showing the evolution to {112}A terminated triangle shape from the hexagonal of $GaAs_{1-x}Sb_x$ core. Red and orange arrows represent the growth directions of the shell in ⟨112⟩B and {110} direction, respectively. The growth rate in the ⟨112⟩A directions is nearly zero. Black lines show the formation process of {112}A facets, until finally developing into a triangular shape. b) Atomic model shows the cross section in (a) projected along the [1-10] direction. On the {112} facets, there are extra Ga(In) dangling bonds on the A-polar facet (indicated as A-site). In comparison, B-polar {112} facets have extra As(Sb or P) dangling bonds, displayed as B-site. This dangling bonds difference results in different surface properties between A- and B-polar {112} facets. In the presence of Sb surfactant, this difference leads to the formation of InP shell only on the B-polar {112} facets.

Because of surface diffusion, surface reconstructions and nucleation kinetics depend directly on the growth parameters. Hence, it is reasonable to assume that the shell morphology can be tuned by changing the InP growth conditions. Indeed, InP shells have been shown to present {110} facets on InP core at low growth temperatures and larger V/III ratios while {112} facets form at high temperatures and low V/III ratios.[54] In an attempt to obtain {110} facets of the InP shell to fully cover the $GaAs_{1-x}Sb_x$ core, several suitable growth conditions for InP shell with {110} facets were investigated. For instance, at a slightly lower temperature (525 °C) and larger V/III ratio (2000), still no growth along the ⟨112⟩A directions is observed and the InP shell thickness in the ⟨110⟩ directions became thinner. In addition, the morphology of the shell is rough. Figure S1 (Supporting Information) shows that a higher growth temperature is also not helpful in overcoming the nucleation barrier in the ⟨112⟩A directions. Instead, high temperature increases the driving force for growth in other directions, leading to faster formation of triangular shape. Increasing the precursor flows is an effective way in increasing local supersaturation and thus has potential to facilitate InP shell growth along A-polar ⟨112⟩ directions. This process is found to only increase the thickness of the InP shell without altering its triangular geometry (see Figure S5b, Supporting Information). Around 3 nm of InP is formed on the {112}A surface, which is about the same in some of the NWs where InP shell is grown for 40 min at standard conditions. Various other shell growth conditions have also been tested without success in stabilizing the {110} or {112}B facets, suggesting that the Sb surfactant induced {112}A terminated InP shell growth is too dominant to be overcome under the standard growth parameter space.

From the above analysis, during the InP shell growth, the existing trace amount of Sb (as seen in Figure 2c) could adsorb on the side facets and form a "floating" (surfactant) layer, effectively reducing the surface energy of NW facets and the driving force for shell growth as a consequence.[35] Moreover, this effect can be facet dependent. According to the shape of $GaAs_{1-x}Sb_x$/InP core/shell structure, the surface energy sequence as a result of the surfactant effect of Sb is deduced as: $\gamma_{\{112\}A} < \gamma_{\{110\}} < \gamma_{\{112\}B}$. The minimum surface energy of A-polar {112} facets could be due to the presence of Ga (or In) dangling bonds (see Figure 3b) which facilitate easier adsorption of Sb by forming Ga—Sb (In—Sb) chemical bonds. In addition, segregation of Sb on the surface could block nucleation sites and inhibit P and In atoms from nucleating.[35,36] At the beginning of shell growth, this restriction on the {112}A surface is so strong that In and P adatoms could not form an InP nucleus before re-evaporating or migrating to {110} or {112}B surface where nucleation is faster. Until a nearly triangular shape is formed, adatoms diffusion process is minimized and if shell growth continues after that, InP nucleation on the {112}A facets becomes possible, albeit very slowly (see Figure S5b, Supporting Information).

Sb, similar to other surfactant elements, is effective in reducing the surface energy and therefore suppresses the crystal growth rate in certain crystallographic directions. However, formation of triangular {112}A side facets are not unique to this nanowire material system. Indeed, it was reported recently that Sn can stabilize {112}A facets during the Sn-seeded GaAs nanowire growth, in contrast to the predominant {112}B side facets generally found for Au-nucleated GaAs nanowires.[43] Note that when considering the droplet/vapor and droplet/nanowire interfaces, it was shown previously that the surfactant role of Sb is effective in drastically narrowing the growth windows for Sb-containing III–V nanowires, making it extremely challenging to grow indefinitely long and narrow nanowires.[23,36,55,56] Even the surfactant properties of elements, such as Sn, Sb, and Zn, are general and will drastically affect growth in all cases, the balance of surface and interface energies can be affected by a number of other parameters as well, which can limit the surfactant-driven growth anisotropy. Such parameters include investigated semiconductor material system, crystal facets, crystal structure, and growth conditions. For example, Sn is found to stabilize {111} side facets during InP shell growth[54] instead of {112}A facets induced by Sb found in this work. Therefore, the surfactant role of Sb in forming triangular morphology could be rather specific to $GaAs_{1-x}Sb_x$/InP nanowire system. Even in Sb-related III–V nanowires, the Sb surfactant effect can have a different influence, since GaSb/InAsSb core/shell nanowires show a hexagonal cross-sectional shape bounded by {110} side facets.[57] Exploration of the influence of surfactants in radial growth but also in axial modes is thought to be highly promising in unlocking new geometries and properties.

2.3. Superior Optical Qualities

Having discussed extensively the structural and morphological properties of the core–shell heterostructures we now turn to their optical properties. **Figure 4**a compares PL emission of core and core/shell nanowires with two different Sb compositions in the core: $GaAs_{0.71}Sb_{0.29}$ and $GaAs_{0.56}Sb_{0.44}$. The PL emission intensity is rather low and noisy for the core-only samples (Figure 4a). In comparison, the PL results of the core/shell nanowires show a strong emission in the near-infrared range, peaking at 1.32 and 1.48 μm, respectively, for the two compositions considered. Quantitatively, the PL intensity of both core/shell nanowire samples is improved more than 100 times over that of the bare core NWs for the most of the NWs. It is worth mentioning that the strong improvement of the PL emission is achieved even with an incomplete passivation of the core surfaces by the InP shell. We expect that the superior optical emission of the $GaAs_{1-x}Sb_x$/InP core/shell nanowires could be further enhanced if the core was fully covered with InP shell. However, full coverage of the sidewalls could be challenging to engineer, in view of the many attempts at tuning the shell morphology under different growth conditions (see Figures S1 and S5, Supporting Information). Around 37 meV redshift of the $GaAs_{0.71}Sb_{0.29}$/InP emission from the core emission is observed, which is ascribed to the presence of tensile strain in the core. A slightly blueshift of the PL emission for the $GaAs_{0.56}Sb_{0.44}$/InP core/shell nanowires compared with the $GaAs_{0.56}Sb_{0.44}$ core-only nanowires is observed, which may be due to a reduction of the Sb content in the core during the shell growth as a result of interdiffusion at higher shell growth temperature. Power-dependent PL from the $GaAs_{0.71}Sb_{0.29}$/InP core/shell nanowire is shown in Figure 4b. A slight blueshift (13 meV) is observed over the excitation power range from 20 to 1450 μW. One likely reason for the blueshift of emission

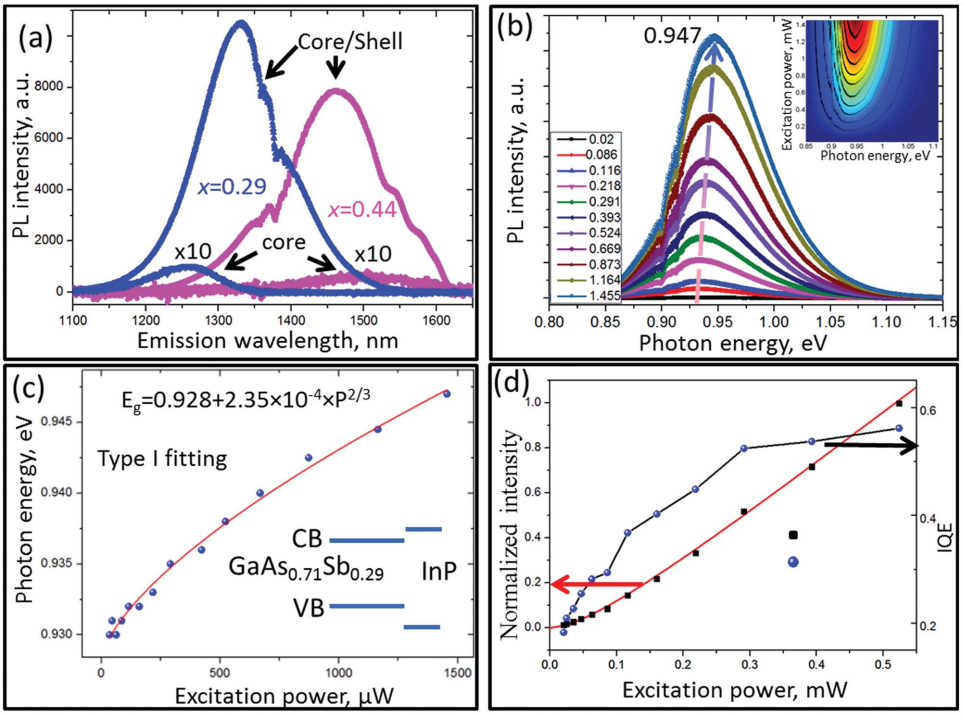

Figure 4. Room temperature PL data of GaAs$_{1-x}$Sb$_x$/InP core/shell NWs. a) Comparison of the PL emission of the core only and core/shell nanowires with two Sb compositions: GaAs$_{0.71}$Sb$_{0.29}$ and GaAs$_{0.56}$Sb$_{0.44}$. The PL intensities of the core only NW are amplified ten times for visibility. b) Power-dependent PL results of GaAs$_{0.71}$Sb$_{0.29}$/InP. A slight blueshift is observed with excitation power. Inset is a false emission intensity map for the power-dependent PL results. The unit of the excitation power is mW. c) Comparison of the measured and calculated peak PL position for type-I bandgap alignment as a function of excitation power. The agreement between fitting and experimental results indicates that the band alignment between core and shell is type I. d) Fitted normalized integrated intensity with excitation power and extracted quantum efficiency of GaAs$_{0.71}$Sb$_{0.29}$/InP NWs obtained from the power-dependent PL spectrum in (b).

spectrum is the filling of the bands caused by an increase of carrier density at high excitation power, which is known as Burstein–Moss (BM) effect.[58] The BM effect can be simplified and written as

$$E_g = E_{g0} + A \times P^{2/3} \quad (1)$$

where E_g is the emission energy, E_{g0} is the bandgap of semiconductor, parameter A is a fitting constant, and P is the excitation power intensity. The fitted peak emission position using BM effect[58] agrees well with the measured results (Figure 4c), indicating that both electron and holes are confined in the core and the observed spectrum blueshift is due to band filling in the core (BM effect). Therefore, this implies that the band alignment between GaAs$_{0.71}$Sb$_{0.29}$ core and InP shell is of type I in nature.

The IQE of a semiconductor is a quantitative parameter that can be used to assess the optical quality of nanowires.[4] The IQE of the core/shell nanowires can be extracted from the dependence of the integrated PL emission intensity with excitation power according to the method introduced by Yoo et al.[59] The experimental normalized integrated PL intensity can be fitted well using this procedure and is shown in Figure 4d. From this fitting, the IQE of the core/shell nanowire is 18% at low excitation power (24 μW) and increases quickly to 56% at 560 μW. The calculated high IQE of the core/shell NW is consistent with its efficient PL emission. The superior optical quality of the core/shell nanowire is due to its high crystal quality (coherent ZB twin-free core/shell structure) and passivation effect offered by the InP shell, which makes it a suitable candidate for applications in the near-infrared range and telecommunications field. For GaAs$_{0.56}$Sb$_{0.44}$/InP NW, IQE is not calculated, because the response of the InGaAs photodetector in our system deteriorates rapidly above 1500 nm. Since PL spectrum is under a redshift with reducing excitation power, quantifying the integrated PL intensity to extract the IQE would be inaccurate. However, since the peak intensity of GaAs$_{0.56}$Sb$_{0.44}$/InP core/shell NW is similar to that of the GaAs$_{0.71}$Sb$_{0.29}$/InP core/shell NW, it is expected that IQE of GaAs$_{0.56}$Sb$_{0.44}$/InP NW would also be relatively high.

The dramatic increase in PL intensity for the GaAs$_{1-x}$Sb$_x$/InP core–shell NWs over the GaAs$_{1-x}$Sb$_x$ bare core suggests a strong reduction in nonradiative recombination at the surface of the NWs. Transient Rayleigh scattering (TRS) spectroscopy has been shown to be a powerful technique to study the band structure, carrier thermalization dynamics, and carrier lifetime of single nanowires.[60–62] The change of polarized Rayleigh scattering efficiency from the nanowire is defined as

$$dR'/R' = \Delta(R_{//} - R_{\perp}) / (R_{//} - R_{\perp}) \quad (2)$$

where $R_{//}$ ($R_{\perp}$) represents the back-reflected Rayleigh scattering of the nanowire with incident light polarized parallel

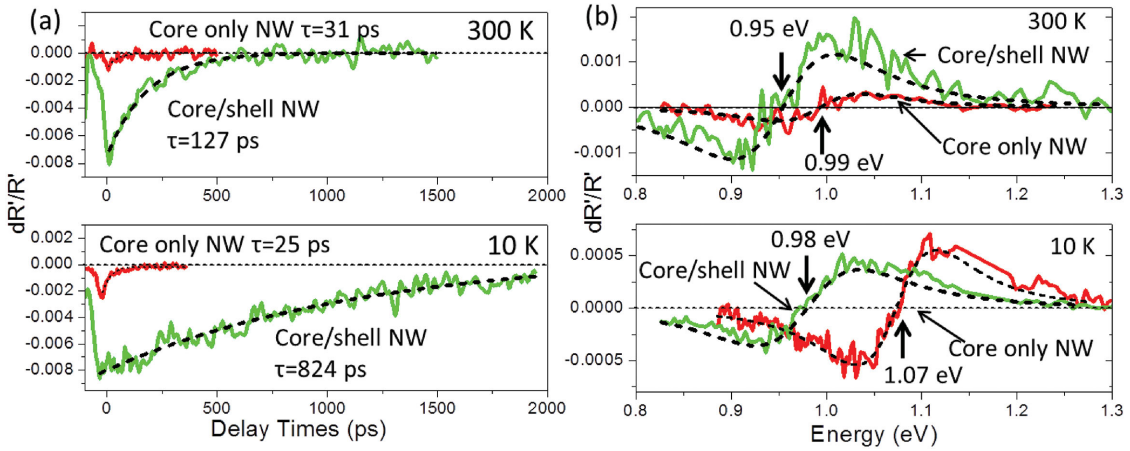

Figure 5. Transient Rayleigh scattering spectroscopy measurements of $GaAs_{0.71}Sb_{0.29}$ and $GaAs_{0.71}Sb_{0.29}$/InP NWs at both 10 and 300 K. a) Time decay of polarized scattering, dR'/R', on the low energy side of the bandgap energy. b) Energy dependence of the polarized scattering efficiency, dR'/R', at late delay times (≈1000 ps after the pump pulse).

(perpendicular) to the nanowire. $R' = R_{//} - R_{\perp}$ is the polarized Rayleigh scattering of nanowire. Polarized Rayleigh scattering with and without photoexcited carriers is measured by the scattering of a delayed fast probe pulse which is tunable from 950 to 1550 nm. By measuring dR'/R' as a function of time after photoexcitation and as function of incident photon energy (probe energy), both the carrier lifetime and bandgap of the nanowire can be determined. For the time decay measurements, the probe energy is fixed at the lower energy side (≈65 meV lower) of the bandgap energy to obtain a signal which is directly proportional to the carrier density. The measured TRS results of $GaAs_{0.71}Sb_{0.29}$ core and core/shell NW both at 300 and 10 K are shown in **Figure 5**. The positive impact of the InP shell is clearly apparent. Indeed, core-only NWs show system limited lifetimes of ≈25 ps at 10 K and ≈31 ps at 300 K. These short lifetimes indicate the strong nonradiative SRV of the $GaAs_{1-x}Sb_x$ core. After passivation with InP shell, carrier lifetimes are enhanced to ≈800 and ≈100 ps at 10 and 300 K, respectively. Assuming that these lifetimes are limited by nonradiative recombination at the surface or heterointerface, the upper limit of SRV (S_{max}) can be calculated by the equation[63]

$$1/\tau_{nr} = 4S_{max}/d \quad (3)$$

where d is the diameter of the NW and τ_{nr} is the nonradiative carrier lifetime. With an average diameter of the NWs taken as ≈100 nm, S_{max} of the $GaAs_{0.71}Sb_{0.29}$ core at 10 K is ≈100 000 cm s^{-1}, while that for the $GaAs_{0.71}Sb_{0.29}$/InP core–shell NW is ≈3000 cm s^{-1} which is comparable to that of the well-established GaAs/AlGaAs NWs.[63] This suggests that InP shell is extremely effective in suppressing the surface states of $GaAs_{1-x}Sb_x$ core, which is consistent with the strong increase in PL efficiency observed in Figure 4d.

To measure the bandgap of these NWs, we tune the pump-probe delay time to 1000 ps where the photoexcited carrier concentration is extremely low, and measure the energy dependence of the polarized scattering efficiency. Such spectra provide a derivative spectrum very similar to photoreflectance spectroscopy, with a zero crossing at the bandgap energy.[60] The bandgap can be directly extracted from the center of the derivative-like dR'/R' spectrum at late times when most of the excited carriers reside close to the band edges. Using a simplified dR'/R' model based on Lorentz oscillator deduced dielectric function,[60] we extract the bandgap of core-only $GaAs_{0.71}Sb_{0.29}$ NWs to be 1.07 and 0.99 eV at 10 and 300 K, respectively, as shown in Figure 5b. These values are consistent with the measurements by PL. After passivation by the InP shell, the bandgap energy of the NW core is redshifted to 0.98 and 0.95 eV at 10 and 300 K, respectively. This is also consistent with the observed PL in these nanowires (Figure 4b), and likely as a result of tensile strain in the core caused by the InP shell.

3. Conclusions

In conclusion, we report the successful growth of coherent ZB twin-free $GaAs_{1-x}Sb_x$/InP core/shell nanowire with unexpected triangular A-polar {112} side facets and high optical quality. We demonstrate how the surfactant role of Sb can tune the shape and the polarity of InP shell, by inhibiting growth in the ⟨112⟩A directions. These findings suggest that surfactant treatment is an effective way to push nanowire growth engineering into new regimes. The possible benefits of Sb surfactant induced triangular geometry are numerous. First, the slow shell growth rate would be very helpful in accurately controlling the quantum well thickness for nanowire quantum well tube growth. Second, the specific shape and facets, for instance, a triangular shape with {112}A facets, can serve as a template for selective growth of quantum dots and quantum wells. Moreover, changing the nanowire cross section from hexagonal to triangular provides a new opportunity for engineering the optical modes and thus tailoring the optical properties, such as absorption and polarization of the emission. In hybrid metal coated semiconductor nanowires, the triangular shape of nanowires will affect the photonic or plasmonic mode confinement profile and thus have some notable advantages in fabricating plasmonic cavities.[64,65] The $GaAs_{1-x}Sb_x$/InP core/shell nanowires with various Sb contents in the core show strong photoemission between 1.3 and

1.5 μm at room temperature. In addition, the NWs have an IQE of 56% with carrier lifetime of ≈100 ps (room temperature) and ≈800 ps (10 K), which makes them promising for device applications in the near-infrared range and telecommunications field.

4. Experimental Section

The $GaAs_{1-x}Sb_x$ NW core was grown on a GaAs stem at 500 °C for 90 min. The growth details can be found in Section S1 (Supporting Information). In short, growth conditions were carefully chosen to synthesize ZB twin-free structure with two different Sb compositions: $GaAs_{0.71}Sb_{0.29}$ and $GaAs_{0.56}Sb_{0.44}$. After growing the nanowire core, the growth conditions were changed to favor a radial InP shell growth. Larger V/III ratio and higher temperature are found to help the formation of a smooth InP shell (see Figure S1, Supporting Information). The optimized InP shell growth conditions were chosen as follows: 550 °C, V/III = 1000, TMIn = 0.6746×10^{-5} mol min^{-1} and growth time, t = 16 min, since these conditions provided a smooth InP shell formation for both $GaAs_{0.71}Sb_{0.29}$ and $GaAs_{0.56}Sb_{0.44}$. Directly switching to InP shell growth after the $GaAs_{0.56}Sb_{0.44}$ growth leads to the Au seeds crawling back to the sidewalls of the core NW. In contrast, this does not happen for cores with lower Sb content ($GaAs_{0.71}Sb_{0.29}$). This phenomenon is caused by the instability of the gold seeds, unpinning from their main {111}B surface and wetting the sidewalls under Sb-rich flows, as observed in our previous publication.[23] Therefore, after growth of $GaAs_{0.56}Sb_{0.44}$ core for 90 min, $GaAs_{0.71}Sb_{0.29}$ with lower Sb content was grown on top of $GaAs_{0.56}Sb_{0.44}$ for 4 min before growth conditions were switched to InP shell growth with the purpose of maintaining the Au sitting on the top of the NWs during InP shell growth. Note that the additional $GaAs_{0.71}Sb_{0.29}$ segment has virtually no growth around the core but only stabilizes the Au seeds on the top (111)B facet prior to InP shell growth (Figure 2b shows there is no additional As-rich layer at the interface and Figure 2e,f does not show any strain between the core and shell that would otherwise result from the mismatched $GaAs_{0.71}Sb_{0.29}$).

The morphology and crystal structure of the core/shell nanowire were characterized using SEM (Zeiss Ultraplus) operated at 5 kV, and TEM (JEOL 2100F). The composition profile of the nanowire was determined by EDX spectroscopy under scanning transmission electron microscopy (STEM) mode. Nanowires were transferred for TEM characterization by gently scratching the nanowire on the substrate using a lacey carbon copper grid. To reveal the details of the core/shell structure, cross-sectional TEM samples were prepared by first embedding the NWs in resin. Then cross-sectional 40 nm thick lamella was sliced from the NWs using an ultramicrotome method.[44] Microphotoluminescence measurements on single nanowire were performed at room temperature. The NW was excited using a 632 nm continuous wave (CW) laser and the emission was detected with a linear InGaAs p-i-n photodetector array. For TRS experiments,[60–62] NWs were dispersed onto a marked Si substrate and placed onto the copper cold finger of a constant helium flow cryostat. The NW was photoexcited by a pump pulse (550 nm) extracted from a Fianium supercontinuum source. The repetition rate of the laser was 20 MHz.

Supporting Information

Supporting Information is available from the Wiley Online Library or from the author.

Acknowledgements

The Australian Research Council is acknowledged for financial support. Access to facilities used in this work was made possible through the Australian National Fabrication Facility, ACT Node, and Australian Microscopy and Microanalysis Research Facility. Y. Wang, H. E. Jackson, and L. M. Smith acknowledge the financial support of the National Science Foundation through Grant Nos. DMR-1105362, ECCS-1100489, and ECCS-1509706.

Received: April 12, 2015
Revised: June 24, 2015
Published online: July 27, 2015

[1] K. Tomioka, M. Yoshimura, T. Fukui, *Nature* **2012**, *488*, 189.
[2] A. W. Dey, J. Svensson, M. Ek, E. Lind, C. Thelander, L. E. Wernersson, *Nano Lett.* **2013**, *13*, 5919.
[3] I. van Weperen, S. R. Plissard, E. P. A. M. Bakkers, S. M. Frolov, L. P. Kouwenhoven, *Nano Lett.* **2013**, *13*, 387.
[4] Q. Gao, D. Saxena, F. Wang, L. Fu, S. Mokkapati, Y. Guo, L. Li, J. Wong-Leung, P. Caroff, H. H. Tan, C. Jagadish, *Nano Lett.* **2014**, *14*, 5206.
[5] S. Assali, I. Zardo, S. Plissard, D. Kriegner, M. A. Verheijen, G. Bauer, A. Meijerink, A. Belabbes, F. Bechstedt, J. E. M. Haverkort, E. P. A. M. Bakkers, *Nano Lett.* **2013**, *13*, 1559.
[6] N. Jiang, Q. Gao, P. Parkinson, J. Wong-Leung, S. Mokkapati, S. Breuer, H. H. Tan, C. L. Zheng, J. Etheridge, C. Jagadish, *Nano Lett.* **2013**, *13*, 5135.
[7] K. Tomioka, T. Tanaka, S. Hara, K. Hiruma, T. Fukui, *IEEE J. Sel. Top. Quantum Electron.* **2011**, *17*, 1112.
[8] D. Saxena, S. Mokkapati, P. Parkinson, N. Jiang, Q. Gao, H. H. Tan, C. Jagadish, *Nat. Photonics* **2013**, *7*, 963.
[9] T. P. H. Sidiropoulos, R. Roder, S. Geburt, O. Hess, S. A. Maier, C. Ronning, R. F. Oulton, *Nat. Phys.* **2014**, *10*, 870.
[10] S. Jahangir, T. Frost, E. Stark, S. Deshpande, P. Bhattacharya, presented at *Device Research Conf. (DRC)*, Santa Barbara, CA, USA, 22–25 June **2014**, p35.
[11] J. Wallentin, N. Anttu, D. Asoli, M. Huffman, I. Åberg, M. H. Magnusson, G. Siefer, P. Fuss-Kailuweit, F. Dimroth, B. Witzigmann, H. Q. Xu, L. Samuelson, K. Deppert, M. T. Borgström, *Science* **2013**, *339*, 1057.
[12] P. Krogstrup, H. I. Jorgensen, M. Heiss, O. Demichel, J. V. Holm, M. Aagesen, J. Nygard, A. Fontcuberta, I. Morral, *Nat. Photonics* **2013**, *7*, 306.
[13] G. Mariani, A. C. Scofield, C.-H. Hung, D. L. Huffaker, *Nat. Commun.* **2013**, *4*, 1497.
[14] E. Nakai, M. Yoshimura, K. Tomioka, T. Fukui, *Jpn. J. Appl. Phys.* **2013**, *52*, 055002.
[15] M. Tchernycheva, A. Messanvi, A. de Luna Bugallo, G. Jacopin, P. Lavenus, L. Rigutti, H. Zhang, Y. Halioua, F. H. Julien, J. Eymery, C. Durand, *Nano Lett.* **2014**, *14*, 3515.
[16] E. Dimakis, U. Jahn, M. Ramsteiner, A. Tahraoui, J. Grandal, X. Kong, O. Marquardt, A. Trampert, H. Riechert, L. Geelhaar, *Nano Lett.* **2014**, *14*, 2604.
[17] M. H. H. Alouane, R. Anufriev, N. Chauvin, H. Khmissi, K. Naji, B. Ilahi, H. Maaref, G. Patriarche, M. Gendry, C. Bru-Chevallier, *Nanotechnology* **2011**, *22*, 405702.
[18] R. Anufriev, N. Chauvin, H. Khmissi, K. Naji, J.-B. Barakat, J. Penuelas, G. Patriarche, M. Gendry, C. Bru-Chevallier, *J. Appl. Phys.* **2013**, *113*, 193101.
[19] X. Zhuang, C. Z. Ning, A. Pan, *Adv. Mater.* **2012**, *24*, 13.
[20] M. Heurlin, T. Stankevič, S. Mickevičius, S. Yngman, D. Lindgren, A. Mikkelsen, R. Feidenhans'l, M. T. Borgström, L. Samuelson, *Nano Lett.* **2015**, *15*, 2462.
[21] S. K. Lim, M. J. Tambe, M. M. Brewster, S. Gradečak, *Nano Lett.* **2008**, *8*, 1386.
[22] Y.-N. Guo, T. Burgess, Q. Gao, H. H. Tan, C. Jagadish, J. Zou, *Nano Lett.* **2013**, *13*, 5085.

[23] X. Yuan, P. Caroff, J. Wong-Leung, H. H. Tan, C. Jagadish, *Nanoscale* **2015**, *7*, 4995.
[24] S. Conesa-Boj, D. Kriegner, X.-L. Han, S. Plissard, X. Wallart, J. Stangl, A. Fontcuberta, I. Morral, P. Caroff, *Nano Lett.* **2014**, *14*, 326.
[25] E. Alarcon-Llado, S. Conesa-Boj, X. Wallart, P. Caroff, A. Fontcuberta, I. Morral, *Nanotechnology* **2013**, *24*, 405707.
[26] L. Jastrzebski, J. Lagowski, H. C. Gatos, *Appl. Phys. Lett.* **1975**, *27*, 537.
[27] P. S. Dutta, H. L. Bhat, V. Kumar, *J. Appl. Phys.* **1997**, *81*, 5821.
[28] J. J. Hannah, J. D. Callum, G. Qiang, H. H. Tan, J. Chennupati, L.-H. James, M. H. Laura, B. J. Michael, *Nanotechnology* **2013**, *24*, 214006.
[29] R. Flückiger, R. Lövblom, M. Alexandrova, O. Ostinelli, C. R. Bolognesi, *Appl. Phys. Express* **2014**, *7*, 034105.
[30] R. Novakovic, D. Giuranno, E. Ricci, S. Delsante, D. Li, G. Borzone, *Surf. Sci.* **2011**, *605*, 248.
[31] T. Matsuura, T. Miyamoto, T. Kageyama, M. Ohta, Y. Matsui, T. Furuhata, F. Koyama, *Jpn. J. Appl. Phys.* **2004**, *43*, L605.
[32] E. O. Jin, W. J. Dong, I. J. Wy, H. H. Young, S. J. Hun, S. L. Gang, G. J. Se, M. B. Seon, S. A. Hyung, Y. Min, *J. Korean Phys. Soc.* **2011**, *58*, 1146.
[33] A. Portavoce, I. Berbezier, A. Ronda, *Mater. Sci. Eng. B* **2003**, *101*, 181.
[34] R. E. Algra, M. A. Verheijen, M. T. Borgstrom, L. F. Feiner, G. Immink, W. J. van Enckevort, E. Vlieg, E. P. Bakkers, *Nature* **2008**, *456*, 369.
[35] P. Nimmatoori, Q. Zhang, E. C. Dickey, J. M. Redwing, *Nanotechnology* **2009**, *20*, 6.
[36] E. A. Anyebe, M. K. Rajpalke, T. D. Veal, C. J. Jin, Z. M. Wang, Q. D. Zhuang, *Nano Res.* **2015**, *8*, 1309.
[37] J. Zou, M. Paladugu, H. Wang, G. J. Auchterlonie, Y. N. Guo, Y. Kim, Q. Gao, H. J. Joyce, H. H. Tan, C. Jagadish, *Small* **2007**, *3*, 389.
[38] S. G. Ghalamestani, M. Heurlin, L. E. Wernersson, S. Lehmann, K. A. Dick, *Nanotechnology* **2012**, *23*, 285601.
[39] F. Qian, Y. Li, S. Gradecak, H. G. Park, Y. Dong, Y. Ding, Z. L. Wang, C. M. Lieber, *Nat. Mater.* **2008**, *7*, 701.
[40] T. Kuykendall, P. Pauzauskie, S. Lee, Y. Zhang, J. Goldberger, P. Yang, *Nano Lett.* **2003**, *3*, 1063.
[41] M. A. Verheijen, R. E. Algra, M. T. Borgström, G. Immink, E. Sourty, W. J. P. van Enckevort, E. Vlieg, E. P. A. M. Bakkers, *Nano Lett.* **2007**, *7*, 3051.
[42] S. Heun, B. Radha, D. Ercolani, G. U. Kulkarni, F. Rossi, V. Grillo, G. Salviati, F. Beltram, L. Sorba, *Small* **2010**, *6*, 1935.
[43] R. Sun, D. Jacobsson, I. J. Chen, M. Nilsson, C. Thelander, S. Lehmann, K. A. Dick, *Nano Lett.* **2015**, *15*, 3757.
[44] N. Jiang, J. Wong-Leung, H. J. Joyce, Q. Gao, H. H. Tan, C. Jagadish, *Nano Lett.* **2014**, *14*, 5865.
[45] G. Wulff, *Z. Kristallogr. Mineral.* **1901**, *34*, 449.
[46] J. W. Gibbs, *The Collected Works of J. Willard Gibbs*, Longmans, Green, New York, NY, USA **1928**.
[47] H. Kauko, T. Grieb, R. Bjorge, M. Schowalter, A. M. Munshi, H. Weman, A. Rosenauer, A. T. J. van Helvoort, *Micron* **2013**, *44*, 254.
[48] T. J. Kempa, S.-K. Kim, R. W. Day, H.-G. Park, D. G. Nocera, C. M. Lieber, *J. Am. Chem. Soc.* **2013**, *135*, 18354.
[49] J. Arbiol, C. Magen, P. Becker, G. Jacopin, A. Chernikov, S. Schafer, F. Furtmayr, M. Tchernycheva, L. Rigutti, J. Teubert, S. Chatterjee, J. R. Morante, M. Eickhoff, *Nanoscale* **2012**, *4*, 7517.
[50] E. Uccelli, J. Arbiol, J. R. Morante, A. Fontcuberta, I. Morral, *ACS Nano* **2010**, *4*, 5985.
[51] M. Peter, D. Serries, N. Herres, F. Fuchs, R. Kiefer, K. Winkler, K. H. Bachem, J. Wagner, presented at *Int. Symp. on Semiconductors*, Berlin, Germany, 22–26 August, **1999**, p55.
[52] H. J. Joyce, Q. Gao, H. H. Tan, C. Jagadish, Y. Kim, X. Zhang, Y. Guo, J. Zou, *Nano Lett.* **2007**, *7*, 921.
[53] S. El Kazzi, L. Desplanque, X. Wallart, Y. Wang, P. Ruterana, *J. Appl. Phys.* **2012**, *111*, 123506.
[54] M. Heurlin, O. Hultin, K. Storm, D. Lindgren, M. T. Borgström, L. Samuelson, *Nano Lett.* **2014**, *14*, 749.
[55] S. R. Plissard, D. R. Slapak, M. A. Verheijen, M. Hocevar, G. W. G. Immink, I. V. Weperen, S. Nadj-Perge, S. M. Frolov, L. P. Kouwenhoven, E. P. A. M. Bakkers, *Nano Lett.* **2012**, *12*, 1794.
[56] M. Ek, B. M. Borg, J. Johansson, K. A. Dick, *ACS Nano* **2013**, *7*, 3668.
[57] B. Ganjipour, S. Sepehri, A. W. Dey, O. Tizno, B. M. Borg, K. A. Dick, L. Samuelson, L. E. Wernersson, C. Thelander, *Nanotechnology* **2014**, *25*, 425201.
[58] X. Liu, Q. Zhang, J. N. Yip, Q. Xiong, T. C. Sum, *Nano Lett.* **2013**, *13*, 5336.
[59] Y.-S. Yoo, T.-M. Roh, J.-H. Na, S. J. Son, Y.-H. Cho, *Appl. Phys. Lett.* **2013**, *102*, 211107.
[60] M. Montazeri, A. Wade, M. Fickenscher, H. E. Jackson, L. M. Smith, J. M. Yarrison-Rice, Q. Gao, H. H. Tan, C. Jagadish, *Nano Lett.* **2011**, *11*, 4329.
[61] M. Montazeri, H. E. Jackson, L. M. Smith, J. M. Yarrison-Rice, J.-H. Kang, Q. Gao, H. H. Tan, C. Jagadish, *Nano Lett.* **2012**, *12*, 5389.
[62] Y. Wang, H. E. Jackson, L. M. Smith, T. Burgess, S. Paiman, Q. Gao, H. H. Tan, C. Jagadish, *Nano Lett.* **2014**, *14*, 7153.
[63] N. Jiang, P. Parkinson, Q. Gao, S. Breuer, H. H. Tan, J. Wong-Leung, C. Jagadish, *Appl. Phys. Lett.* **2012**, *101*, 023111.
[64] J. P. Kottmann, O. J. F. Martin, *Phys. Rev. B* **2001**, *64*, 235402.
[65] S. Mokkapati, D. Saxena, N. Jiang, L. Li, H. H. Tan, C. Jagadish, *Nano Lett.* **2015**, *15*, 307.